

Control and Integration of a multiphase Brushless Wounded Synchronous Motor Drive

Rémi Perrin, Guilherme Bueno-Mariani
Mitsubishi Electric R&D Centre Europe
1 Allee de beaulieu
Rennes, France

Email: r.perrin@fr.merce.mee.com

Keywords

« Brushless drive », « Control of drive », « Multiphase drive », « Packaging »

Abstract

This paper presents a fully integrated seven-phase Brushless Wounded Rotor Synchronous Motor BWRSM machine drive and its control. A direct integration strategy of the power electronics on the motor case is performed. Advanced PCB integration with embedded die are used for low profile rotary transformer. For the control side, the machine was modelled by Finite Element Method (FEM) in order to extract the flux tables. These tables were then used to improve the precision of analytic simulation model. By using so obtained analytic simulation with integrated flux tables designed field-oriented control was verified. Details on design and the model are presented in the paper. Finally, the controller's efficiency and the power electronics of the motor drive are confirmed with experiments on described prototype machine.

Introduction

HVAC (Heating, ventilation and air-conditioning) is one of the main applications for electrical machines. The machines implemented in these systems are dominantly PMSM (Permanent Magnet Synchronous Machine) because of their high torque density and efficiency. The main disadvantage with this type of machines remains unstable price of rare-earth magnets [23]. Nowadays, other machines appear as potential alternatives to the PMSM [1], [2]. Among the potential candidates, the BWRSM, was identified due to a torque density close to the PMSM [3], [4]. BWRSM has also the advantage of having a wider field weakening region at high speeds in conjunction with a lower cost.

The main advantages of multi-phase machines are known to be reliability, higher torque density, fault tolerance capability and reduced torque pulsation [5]. The motivation of this study is to develop a high integrated BWRSM that could reach the same performances of a PMSM with the advantage of reliability and fault tolerance capability for harsh environments.

Simplified machine modelling is used on many different studies ever since Park transformation theory was introduced. This transformation simplified the studies of transient behavior of the electrical machines, making controlling the machine much easier. Typically, Park transformation allows to turn a 3-phases machine into 2-components (d-q) simplifying the modelling of the machine. However, Park transformation can be applied for any kind of multiphase machine [6] into 2-phases modelling.

Recent improvements in the power density, packaging of power electronics technologies and new semiconductor improvement are opening new opportunities for the integration of more power electronics within the motor case [7], [8]. Motor volume reduction has clear advantages, especially for application with constrained volume, dust sensitive industry [9] and cost reduction due to less interconnection.

This volume reduction is due to the elimination of the need of two separated housing for power electronic and motor as well as the cable connection in between the drive and the motor [10]. The absence of cable connection also goes along a reduction of the total weight of the assembly. In terms of EMI, the use of short connection reduces the propagated noise while issues related to long connection with control signal are mitigated. This results in lowering surge voltages for long cables and slowing down the progressive insulation aging [11], [12] due to non-homogeneous distribution over the windings

Moreover, the opportunity of power electronic integration in the motor comes along new outlooks for optimizing both cost and overall complexity of the system. Placement of power electronics inside the motor case also offers

new opportunities for self-diagnosis and simplifies application of additional functions such as determining rotor position and lifetime prediction [13], [14].

The paper will address first different aspects of the motor drive for this 7 phases BWRSM. In the second section, the model of the machine to be used on the simulations is presented. The main objective is to obtain a simple model of the machine that considers the saturation effect and can be therefore used for control design purposes. The third section presents the control design and design verification by simulation. The fourth section is focused on the power electronics integration on the machine. Some preliminary experimental results are given. Finally, the last section concludes the paper and outlines the future research

Machine modeling

One of the main characteristics of the Park transformation is that the flux linkages are independent of the rotor position. Beyond that the voltage and current are constant when the steady state is achieved. This is the main reason why Park transformation is widely used on the analysis of steady state of electrical machines [4].

The analytical BWRSM model in the Park reference is described by the following equations. This model considers the machine without any damper windings [4].

$$v_d = R_s i_d - \omega \varphi_q (I_d, I_q, i_f) + \frac{d\varphi_d(I_d, I_q, i_f)}{dt} \quad (1)$$

$$v_q = R_s i_q \mp \omega \varphi_d (I_d, I_q, i_f) + \frac{d\varphi_q(I_d, I_q, i_f)}{dt} \quad (2)$$

$$v_f = R_s i_f + \frac{d\varphi_f(I_d, I_q, i_f)}{dt} \quad (3)$$

$$T_{em} = \frac{\gamma p}{2} (\varphi_d I_q - \varphi_q I_d) \quad (4)$$

This model can consider the saturation of the inductances since the Park transformation is merely a geometric transformation. On the next paragraph, the FEM modelling of the machine used to obtain the flux tables with respect to the current is detailed.

A. FEM Modelling

A FEM model was built using FEMM software [15], which provides the low-frequency electromagnetic analysis on two-dimensional planar and axisymmetric problems. From [3], [15]–[17] a 2D FEM model is built for the BWRSM with 7-phase/7-slots/6-poles and concentrated-windings. The results can be found in Fig. 1

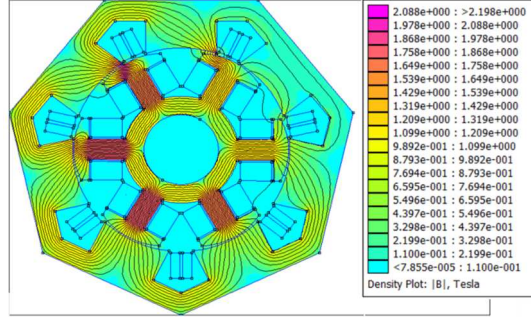


Fig. 1: Simulation model in FEMM

Fig. 1 also shows the simulation results of the machine in FEMM making it is possible to observe the flux lines and the saturation of the machine in different positions.

One weakness of FEMM software is that transient simulation is not available. Making it impossible to co-simulate with the control. Even if this would be achievable, this kind of simulation would be time consuming. In order to overcome this difficulty and obtain a controller simulation model that would consider the saturation of the machine flux tables in function of the current were extracted from the FEMM simulation.

These tables will be used in the analytical machine model. The model considers the fundamental space harmonics component of the air-gap, the flux density and the BEMF (Back Electromotive force). The flux and the current values are measured on the FEMM model and Park transformation is applied in order to obtain a d-q model. This allows the flux to be independent of the rotor position.

Since the position of the rotor does not have any influence on the flux linkages, the simulation procedure to design the flux tables is as follows:

- The position where d axis is aligned with the flux in phase A.
- The current on the rotor is maintained at 5.1A, since constant current on the rotor is predicted.

- I_d and I_q changes from 0 A 20 A
- The corresponding flux linkage φ_d and φ_q are recorded on each point of operation.

As previously mentioned, the Park transformation can be applied for any multiphase machine [6]. For a seven-phase machine Park transformation of the flux can be found on (5), while the Inverse Park transformation for the currents can be found on (6).

$$\begin{bmatrix} \varphi_d \\ \varphi_q \end{bmatrix} = \frac{2}{7} \begin{bmatrix} \cos\theta_m & \cos(\theta_m - \frac{2\pi}{7}) & \dots & \cos(\theta_m - \frac{6\cdot2\pi}{7}) \\ -\sin\theta_m & -\sin(\theta_m - \frac{2\pi}{7}) & \dots & -\sin(\theta_m - \frac{6\cdot2\pi}{7}) \end{bmatrix} \begin{bmatrix} \varphi_a \\ \varphi_b \\ \vdots \\ \varphi_g \end{bmatrix} \quad (5)$$

$$\begin{bmatrix} I_a \\ I_b \\ I_c \\ \vdots \\ I_g \end{bmatrix} = \begin{bmatrix} \cos\theta_m & -\sin\theta_m \\ \cos(\theta_m - \frac{2\pi}{7}) & -\sin(\theta_m - \frac{2\pi}{7}) \\ \cos(\theta_m - \frac{2\cdot2\pi}{7}) & -\sin(\theta_m - \frac{2\cdot2\pi}{7}) \\ \vdots \\ \cos(\theta_m - \frac{6\cdot2\pi}{7}) & -\sin(\theta_m - \frac{6\cdot2\pi}{7}) \end{bmatrix} \begin{bmatrix} I_d \\ I_q \end{bmatrix} \quad (6)$$

The proposed simulation provides the tables from the relationships $\varphi_d(i_d, i_q)$ and $\varphi_q(i_d, i_q)$. Using a technique presented on [4], the inverted relationship $i_d(\varphi_d, \varphi_q)$ and $i_q(\varphi_d, \varphi_q)$ is obtained and used directly on the control simulation. The two flux tables can be understood as a set of data points $(\varphi_d, \varphi_q, i_d, i_q)$. The independent variables and the dependent variables can be swapped. The flux linkage is considered as the independent variables, the new inverted flux tables of $i_d(\varphi_d, \varphi_q)$ and $i_q(\varphi_d, \varphi_q)$ can be seen in Fig. 2.

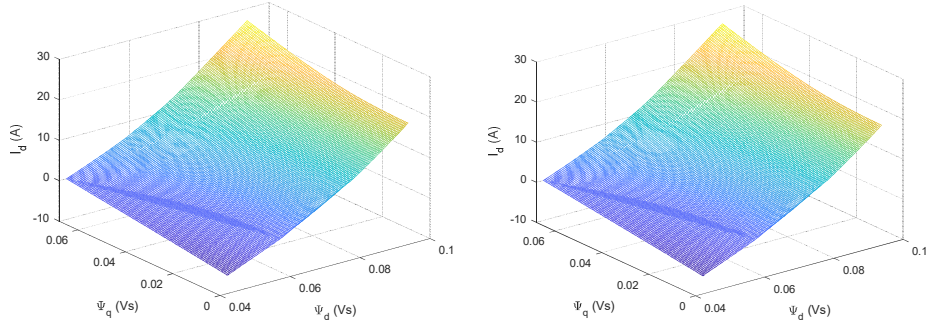


Fig. 2: Inversed flux tables a) $I_d(\varphi_d, \varphi_q)$ and b) $I_q(\varphi_d, \varphi_q)$

The generated look-up table (LUT) $i_d(\varphi_d, \varphi_q)$ and $i_q(\varphi_d, \varphi_q)$ can be used in the machine model for the control simulation, taking into account the saturation of the machine. The proposed block scheme for the model used on the simulation can be found in Fig. 3.

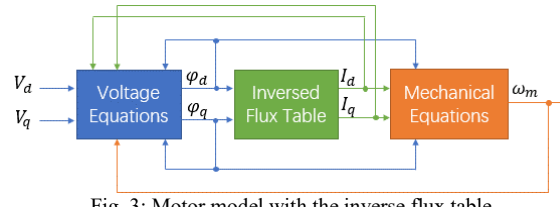


Fig. 3: Motor model with the inverse flux table

II. OPEN LOOP SIMULATION

In this section, the simulation of the open loop control will be detailed, and the results will be presented. The model considers the saturation of the machine by means of the LUT previously built. It also takes into consideration the design of the stator board with the hysteresis controller for the PWM generation.

The controller scheme can be found in Fig. 4.

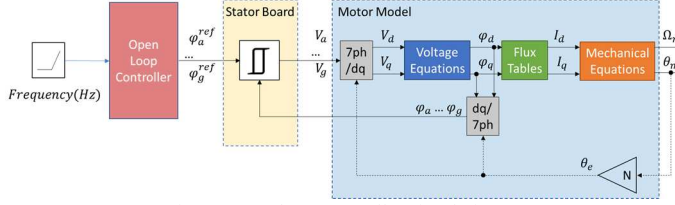


Fig. 4: Open loop controller simulation

Normally open loop control of synchronous machines considers V/f controllers in order to obtain constant φ_d and φ_q . The problem in the case of this integrated machine is that the stator board has already the feedback from the flux in each tooth of the motor from a search coil. This feedback is used on a hysteresis manner in order to generate the needed PWM. In order to be able to control the machine under open loop we need to generate the flux references in the seven phases rather than voltage reference. Instead of V/f controller is a φ/f controller. The amplitude of the flux is maintained at a constant level while the frequency is raised over the time.

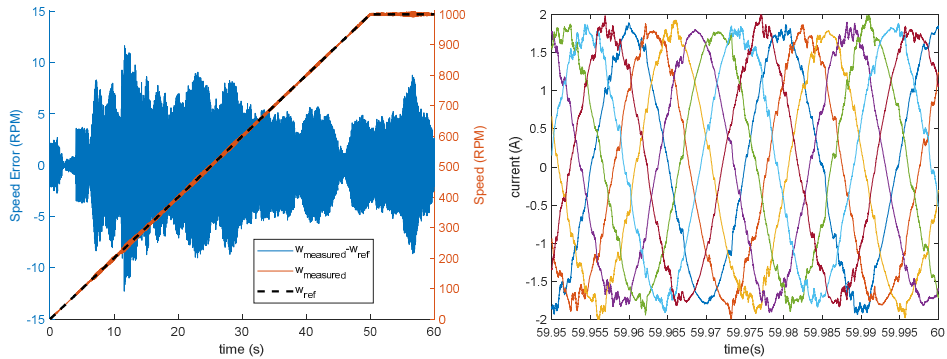


Fig. 5: Speed response to ramp (left) and Current response on the 7 phases (right)

Fig. 5 shows the speed response to slow ramp. This ramp needs to be slow since there is no feed-back on the speed and the machine do not have any kind of starter squirrel cage or damper winding on the rotor. The output speed follows the reference even on open-loop control with minimum error.

The current output when the speed 1000 rpm can be seen in Fig. 5. There are some deformations on the current that are linked to the switching of the 7 inverters and the saturation phenomenon of the machine. These results will be later compared with the experimental results on the next section

Power electronics integration for compact motor drive

Wireless transmission for rotary application is designed to avoid electrical contact for reliability and lifetime improvement. The rotor winding of the BWRSM needs to be energized from the static part. The most common way to supply is through brushes and slip rings [24], [25]. Nevertheless, the slip ring produces carbon dust that restricts the application range excluding clean room environment (medical, food industry). In addition, its lifetime is impeded and a dedicated space is required on the motor what increases the overall volume [26].

Inductive (IPT) and Capacitive (CPT) transfer are two different ways to wirelessly transfer the energy and replace direct electrical contact such as slip ring.

The CPT can be achieved by using a modulation of the electrical field to transfer the energy between two electrodes [27]. This system can be very cost effective compared to an IPT due to the absence of magnetic material and copper windings. The CPT has also the advantage of being more tolerant to misalignment between primary and secondary sides. However, most applications are using the capacitive coupling in a resonant tank that requests a nano-farad range capacitance value. The application is therefore limited to short air-gap leading to a limited capability of withstanding high voltage.

The IPT can be achieved by the magnetic field to transfer the energy in between two coupled coils [28]. IPT is easily implemented with different resonant topologies due to the large leakage inductance coming from a large air-gap. The IPT system can be classified in function of the type of topology, series-series, series-parallel, parallel-series, and parallel-parallel [29]. In the state of the art, the IPT efficiency can be up to 97 % for 7 kW [30]. However, the magnetic core and the copper needed to design the coils increase the cost of the system [31]. In this application, IPT is selected to feed the rotor due to its capability to work with larger air-gap.

A. Rotary Transformer

Rotary transformer design is different than a classical transformer due to its large air-gap to accommodate with the inherent distance between stator and rotor (primary-secondary). Consequently, high values of leakage inductance are usually obtained, along with high magnetizing currents in the case of an inductive transfer.

Parameters	Value
Input Voltage	100 V
Input Current	3 A
Output Voltage	60 V
Output Current	5.1 A
Switching Frequency	100 kHz
Max. Temperature	125°C
Air-gap	1 mm
ZVS	T1 & T2 On and Off
ZCS	Synchronous rectifier MOSFET at Turn-Off

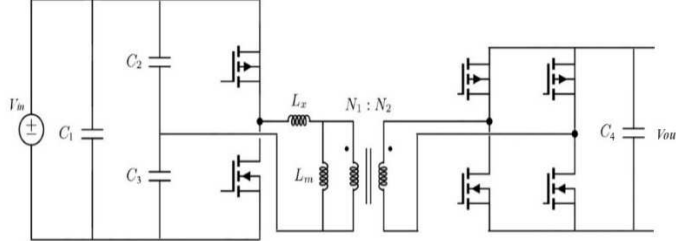


Fig. 6 Series resonant converter input parameters and schematic.

The IPT system includes, a DC/AC source that excites the primary of the rotary transformer with a periodic AC current, the secondary of the transformer that needs an AC/DC rectifier to feed the rotor coils and the respective control electronics. The input parameters for the converter selected are detailed in Fig. 6.

The series resonant topology is able to achieve ZVS (Zero Voltage Switching) on both primary transistors and ZCS (Zero Current Switching) on the synchronous rectifier at turn-off [32], [33]. The resonant tank is made with the leakage inductance of the transformer L_x and the two capacitors C_2 and C_3 . In this case, the tank does not need any additional discrete components which helps keep a low volume and complexity. The half-bridge power stage operates at fixed duty-cycle (50%) and switching frequency (100 kHz), set according to the tank resonant frequency. The control is made through a phase-leg gate driver with a dead-time circuitry and external resistors.

The secondary side of the transformer embeds the synchronous rectifier MOSFETs in the PCB using a stacking method and a process detailed in [34]. This method allows a better optimization of the PCB footprint as well as a lower resistivity of the connection, resulting in lower losses and less thermal stress on the power dies. This point will be fully explained in the following section.

B. Stator Inverters

An H-bridge circuit is used to supply each phase following the reference current. Four MOSFETs with two associate bridge gate drivers and local control are chosen for fitting the parameters in Table I.

Table I: Input parameters

Parameters	Value
Bus Voltage	150 V
Input Current	3.1 A
Maximum ripple bus voltage	5%
Switching Frequency Max	40 kHz
Max Temperature	125°C
Mode	Hard switching
Size Max	55 X 55 mm

The stator control is made in two different parts. The first part is the master control board made with the FPGA. It receives the position and speed information from a rotary encoder and sends a signal equivalent to the current shape expected in the stator coil to the stator board a reference. The reference signal mentioned above is injected in the second control loop, here called as local control loop, based on a hysteresis control type.

As shown in Fig.4, the control principle is based on a hysteresis comparator. The flux reference from the FPGA is compared with the flux measured by the search coil. The low-pass filter is taking the differential input signal from the FPGA board and linearize it to generate the reference signal for the hysteresis comparator. The comparator has two complementary outputs sending those PWM signals directly to the gate driver. The whole control loop circuit is supplied by a symmetrical $\pm 5V$ power supply in order be compliant with the sinusoidal

signal from reference and search coil while keeping a symmetric amplitude on the input signal.

C. Motor Drive Integration

1) Rotary transformer and Smart stator tooth

As shown in [17], the motor design, is the result of a maximum power density optimization. In a similar manner, the volume allocated to the rotary converter and the stator tooth also needs to be reduced. Consequently, the mechanical design of those converters is driven by the compactness. In low power converters, interconnections can be a significant part of the overall volume due to the reduce power conversion area. In order to reduce the impact both sides - primary and secondary side of the converter are made on a single PCB. The windings, the power stage and the control system are in the PCB. On the rotor side, the available volume is even more constrained. In particular, the thickness of the rotating part is limited. One trend in power electronics is to embed the power dies in the PCB. This technology drastically reduces the parasitic inductance in the switching cell, enables double side cooling and improves reliability. One additional advantage of this technology, from which this converter will benefit, is the low-profile shape of the PCB. Both sides of the converter, stator or rotor side, are built symmetrically as shown in Fig. 7. Each PCB, which embeds one side of the transformer, will be surrounded by a magnetic core concentrating the field towards the other PCB. The used material is a mix of epoxy and ferrite powder that can be molded, in any shape then cured to get its final mechanical strength. This assembly is further strengthened by an aluminum yoke. One side of the PCB is flushed with the yoke surface in order to maximize the coupling without any mechanical interference.

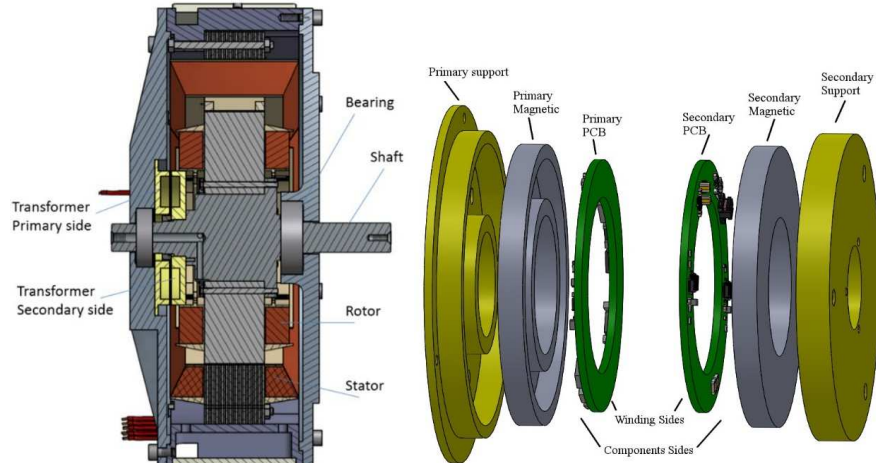


Fig. 7: Cross view of the motor (left) and exploded view of the rotary transformer (right).

Since the transformer is split between the stator and the rotor side, a functional air gap is mandatory. The thickness of this air gap is driven by mechanical constraints and will affect the magnetizing inductance of the transformer. Based on the assembly tolerances and unbalance of parts, the air gap is fixed at 1 mm. As demonstrated in [32], the resonant frequency is fixed by the leakage inductance and capacitors C2 and C3. The switching frequency is mostly limited by the conducting losses in the switches since their intrinsic capacitances are negligible. To set this frequency, the value of the resonant capacitor needs to be selected based on the leakage inductor value.

As shown in Fig. 8, the rotary transformer is placed on the rear of the motor. The secondary side of the transformer is placed in between the shaft and the stator windings. This assembly allows to limit the increase of the length of the back case of the motor. The primary side is fixed on the back case in a cavity. The bearing is on the outside of the transformer in order to reduce the connection complexity between the rotor and the transformer.

As shown in Fig. 8, for the stator tooth integration specific cavity all around the stator within the motor case. Two holes in the bottom of the cavity allow the connection with the search coil, used for the motor control, and the stator coil on the other side. A cable path is drilled all around the motor case to make the connection easier in between the 7 phases. The PCB has an interface to connect the thermal pad against the lid of the stator slot in order to extract heat from the MOSFETs bridge. The interface is a bit higher than the decoupling capacitor and is fixed with 4 screws in between the lid and the PCB board.

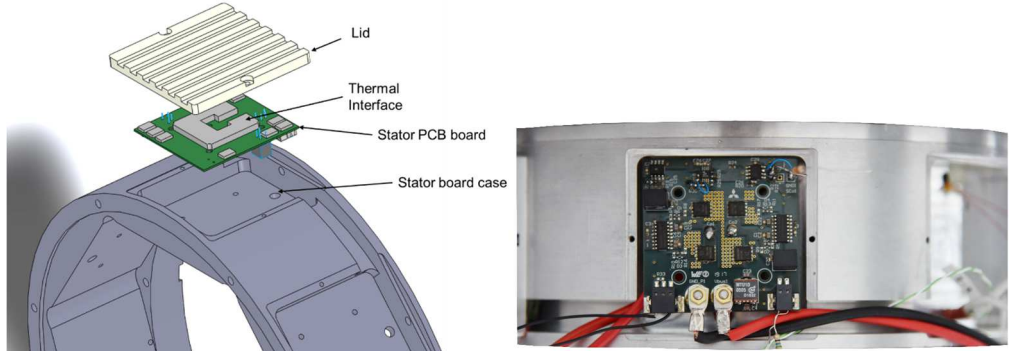


Fig. 8: Assembly view (top) and picture (bottom) of the PCB board the lid on the motor case

2) Manufacturing of the rotary transformer

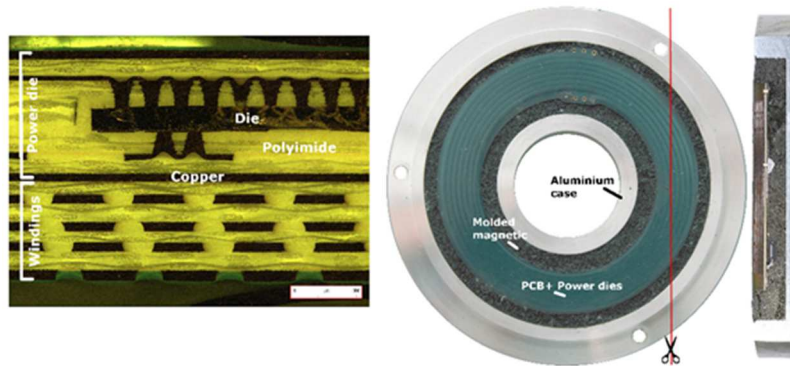


Fig. 9: Cross section of the PCB and of the transformer after potting

On the rotary transformer side, four silicon N-MOSFETs from Infineon were embedded in a polyamide substrate (Arlon 35N) in order to withstand the high temperature ($T_j=160^\circ\text{C}$) with $70 \mu\text{m}$ copper layers. The top circuit components are soldered following a standard process in order to realize the synchronous rectifier function associated with the four transistors embedded. The PCB populated is then embed in an epoxy molded magnetic material within an aluminum container. A picture of the final assembly is shown in Fig. 9.

The transformer is characterized in order to adapt the resonant tank to the right leakage inductance value. The magnetizing inductance at primary is measured with an impedance meter at the primary and secondary are $695 \mu\text{H}$, $449 \mu\text{H}$ for respectively, and $110 \mu\text{H}$ for the leakage. Those values confirm the poor coupling factor and prove the necessity of a resonant topology.

3) Motor drive experimental test

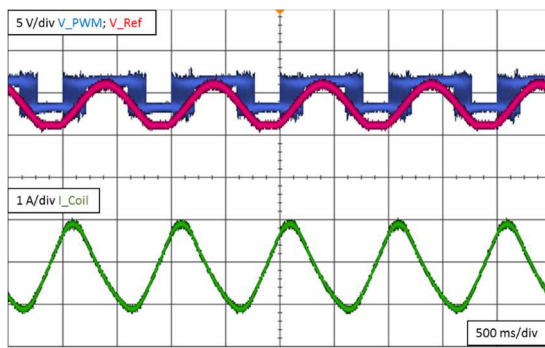


Fig. 10: Sinus reference and the PWM generated accordingly and the stator coil current

The built test bench has a torque meter and the assembled machine was coupled with a load machine. It was driven by a FPGA controller developed for the test, applying speed control in open loop. As described in Fig. , each stator coil is equipped with a search coil for the local hysteresis controller. The flux value is compared to the reference sent by the FPGA to operate the local hysteresis controller. The search coil value is converted into a flux by the mean of an integrator directly on each stator inverter. This control architecture gives redundancy to the machine and helps with operating under fault. A ramp from 0 to 1000 rpm is applied on the control and the rotary

transformer supplies the rotor coils with 5 A showed in Fig. . The rotary transformer and the machine showed the predicted behavior at the operating point. The rotary transformer was successful in its purpose to be a “transparent” replacement for slip ring system.

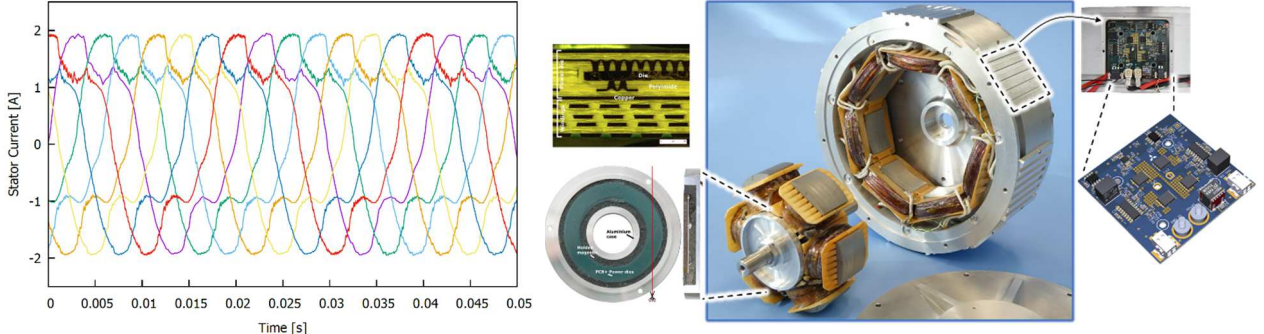


Fig. 11: Seven stator currents and final assembly of the BWRSM motor

The current on the motor at 1000 rpm operating with the open loop control is shown in Fig. 11 as well as the final assembly process. The simulation presents the same amplitude for the currents but there a phenomenon of deformation on the seven phase currents that is not predicted from the simulation.

Conclusion

In this paper the FEM modelling of a BWRSM was discussed with the goal of control simulation. The model turned out to be effective for the modelling of nonlinear saturation of the machine. It also made possible to simulate the control with less computational effort than a co-simulation between the FEM simulation and control simulation. The open-loop control is then simulated in MATLAB/SIMULINK using the previous cited BWRSM model. In a second step a 350 W rotary transformer with PCB embedded dies is designed and implemented in a 3.3 kW BWRSM. A 100 kHz series resonant topology circuit design for the converter is given, as well as the rotary transformer and the smart stator tooth assembly structure. The result is an optimized structure for a brushless motor drive in a volume constrained motor context. Final experimentation shows the motor drive with the rotary transformer, its converter and the smart stator tooth within the motor case both control in open loop up to 1000 rpm.

References

- [1] R. Parsons, “Things in Motion: How to model a BLDC (PMSM) motors Kv (velocity constant) and Kt (torque constant) in FEMM,” *Online*, 2019. <https://things-in-motion.blogspot.com/2019/02/how-to-model-blcd-pmsm-motors-kv.html> (accessed Dec. 15, 2020).
- [2] D. C. Meeker, “Rotating Losses in a Surface Mount Permanent Magnet Motor:Finite Element Method Magnetics,” *Online*, 2017. <http://www.femm.info/wiki/SPMLoss> (accessed Dec. 15, 2020).
- [3] H. T. LE LUONG, “Optimal Design of Modular High Performance Brushless Wound RotorSynchronous Machine for embedded systems,” *PhD Thesis, Univ. Toulouse*, no. Umr 5215, pp. 1–190, 2010.
- [4] T. Wisniewski, J. C. Vannier, B. Lorcen, J. Saint-Michel, and X. Jannot, “Wound-rotor synchronous machine dq modeling with saturation for transient analysis,” *2017 IEEE Int. Electr. Mach. Drives Conf. IEMDC 2017*, pp. 11–16, 2017, doi: 10.1109/IEMDC.2017.8002063.
- [5] L. Parsa, “On advantages of multi-phase machines,” in *IECON Proceedings (Industrial Electronics Conference)*, 2005, vol. 2005, pp. 1574–1579, doi: 10.1109/IECON.2005.1569139.
- [6] A. A. Rockhill and T. A. Lipo, “A generalized transformation methodology for polyphase electric machines and networks,” *Proc. - 2015 IEEE Int. Electr. Mach. Drives Conf. IEMDC 2015*, pp. 27–34, 2016, doi: 10.1109/IEMDC.2015.7409032.
- [7] N. R. Brown, T. M. Jahns, and R. D. Lorenz, “Power Converter Design for an Integrated Modular Motor Drive,” *Ind. Appl. Conf. 2007. 42nd IAS Annu. Meet. Conf. Rec. 2007 IEEE*, pp. 1322–1328, 2007, doi: 10.1109/07IAS.2007.205.
- [8] P. Brockerhoff, Y. Burkhardt, K. Egger, and H. Rauh, “Highly integrated drivetrain solution: Integration of motor, inverter and gearing,” *2014 4th Int. Electr. Drives Prod. Conf. EDPC 2014 - Proc.*, 2014, doi: 10.1109/EDPC.2014.6984412.
- [9] “Motors/generators for traction/propulsion applications: A review - IEEE Journals & Magazine.” <https://ieeexplore.ieee.org/document/6470756> (accessed Feb. 04, 2021).
- [10] J. Wang, Y. Li, and Y. Han, “Integrated Modular Motor Drive Design With GaN Power FETs,” *IEEE Trans. Ind. Appl.*, vol. 51, no. 4, pp. 3198–3207, 2015, doi: 10.1109/TIA.2015.2413380.

- [11] M. Kaufhold, H. Auinger, M. Berth, J. Speck, and M. Eberhardt, "Electrical stress and failure mechanism of the winding insulation in PWM-inverter-fed low-voltage induction motors," *IEEE Trans. Ind. Electron.*, vol. 47, no. 2, pp. 396–402, 2000, doi: 10.1109/41.836355.
- [12] P. Wang, G. C. Montanari, and A. Cavallini, "Partial discharge phenomenology and induced aging behavior in rotating machines controlled by power electronics," *IEEE Trans. Ind. Electron.*, vol. 61, no. 12, pp. 7105–7112, Dec. 2014, doi: 10.1109/TIE.2014.2320226.
- [13] I. Vernica, H. Wang, and F. Blaabjerg, "Uncertainties in the Lifetime Prediction of IGBTs for a Motor Drive Application," in *Proceedings - 2018 IEEE International Power Electronics and Application Conference and Exposition, PEAC 2018*, Dec. 2018, doi: 10.1109/PEAC.2018.8590417.
- [14] F. Barbieri, J. W. Hines, M. Sharp, and M. Venturini, "Sensor-Based Degradation Prediction and Prognostics for Remaining Useful Life Estimation: Validation on Experimental Data of Electric Motors," 2015.
- [15] H. T. Le Luong, F. Messine, C. Héniaux, G. Bueno Mariani, N. Voyer, and S. Mollov, "Comparison between fmincon and NOMAD optimization codes to design wound rotor synchronous machines," in *International Journal of Applied Electromagnetics and Mechanics*, 2019, doi: 10.3233/JAE-191108.
- [16] H. T. Le Luong, C. Héniaux, F. Messine, G. Bueno-Mariani, N. Voyer, and S. Mollov, "Finite element analysis of a modular brushless wound rotor synchronous machine," *J. Eng.*, vol. 2019, no. 17, pp. 3521–3526, 2019, doi: 10.1049/joe.2018.8206.
- [17] H. T. Le Luong, F. Messine, C. Héniaux, G. B. Mariani, N. Voyer, and S. Mollov, "3D Electromagnetic and thermal analysis for an optimized wound rotor synchronous machine," *Proc. - 2018 23rd Int. Conf. Electr. Mach. ICEM 2018*, pp. 455–460, 2018, doi: 10.1109/ICELMACH.2018.8507020.
- [18] C. H. v. d. Broeck, "Lecture 9 Modeling And Current Control." RWTH Aachen University, 2019.
- [19] J. Espina, A. Arias, J. Balcells, and C. Ortega, "Speed anti-windup PI strategies review for field oriented control of permanent magnet synchronous machines," *CPE 2009 - 6th Int. Conf. - Compatability Power Electron.*, no. June 2009, pp. 279–285, 2009, doi: 10.1109/CPE.2009.5156047.
- [20] J. Espina, A. Arias, J. Balcells, and C. Ortega, "Speed anti-windup PI strategies review for field oriented control of permanent magnet synchronous machines," in *CPE 2009 - 6th International Conference-Workshop - Compatability and Power Electronics*, 2009, pp. 279–285, doi: 10.1109/CPE.2009.5156047.
- [21] S. Huang, Z. Chen, K. Huang, and J. Gao, "Maximum torque per ampere and flux-weakening control for PMSM based on curve fitting," in *2010 IEEE Vehicle Power and Propulsion Conference, VPPC 2010*, 2010, doi: 10.1109/VPPC.2010.5729024.
- [22] W. Ahmed Khan, "Torque Maximizing and Flux Weakening Control of Synchronous Machines Title: Torque Maximizing and Flux Weakening Control of Synchronous Machines," *Master's Thesis, Aalto Univ.*, p. 63, 2016, [Online]. Available: <https://core.ac.uk/download/pdf/80719727.pdf>.
- [23] A. Chiba, K. Kiyota, N. Hoshi, M. Takemoto, and S. Ogasawara, "Development of a rare-earth-free SR motor with high torque density for hybrid vehicles," *IEEE Trans. Energy Convers.*, vol. 30, no. 1, pp. 175–182, 2015, doi: 10.1109/TEC.2014.2343962.
- [24] R. D. Hall and R. P. Roberge, "Carbon brush performance on slip rings," *IEEE Conf. Rec. Annu. Pulp Pap. Ind. Tech. Conf.*, 2010, doi: 10.1109/PAPCON.2010.5556522.
- [25] Morgan Advanced Materials, "Carbon Brush & Holder Technical Handbook," [Online]. Available: http://www.morganelectricalmaterials.com/media/1996/technicalhandbookglobalproof_0.pdf.
- [26] M. A. Badr, A. I. Alolah, and A. F. Almarshood, "Transient performance of series connected three phase slip-ring induction motors," *IEEE Trans. Energy Convers.*, vol. 13, no. 4, pp. 305–310, 1998, doi: 10.1109/60.736314.
- [27] D. Shmilovitz, S. Ozeri, and M. M. Ehsani, "A resonant LED driver with capacitive power transfer," in *Conference Proceedings - IEEE Applied Power Electronics Conference and Exposition - APEC*, 2014, pp. 1384–1387, doi: 10.1109/APEC.2014.6803487.
- [28] Q. Li and Y. C. Liang, "An Inductive Power Transfer System with a High-Q Resonant Tank for Mobile Device Charging," *IEEE Trans. Power Electron.*, vol. 30, no. 11, pp. 6203–6212, Nov. 2015, doi: 10.1109/TPEL.2015.2424678.
- [29] O. Knecht and J. W. Kolar, "Comparative evaluation of IPT resonant circuit topologies for wireless power supplies of implantable mechanical circulatory support systems," in *Conference Proceedings - IEEE Applied Power Electronics Conference and Exposition - APEC*, May 2017, pp. 3271–3278, doi: 10.1109/APEC.2017.7931166.
- [30] J. Deng, F. Lu, S. Li, T. D. Nguyen, and C. Mi, "Development of a high efficiency primary side controlled 7kW wireless power charger," in *2014 IEEE International Electric Vehicle Conference, IEVC 2014*, 2014, doi: 10.1109/IEVC.2014.7056204.
- [31] J. Deng, F. Lu, W. Li, R. Ma, and C. Mi, "ZVS double-side LCC compensated resonant inverter with magnetic integration for electric vehicle wireless charger," in *Conference Proceedings - IEEE Applied Power Electronics Conference and Exposition - APEC*, May 2015, vol. 2015-May, no. May, pp. 1131–

- 1136, doi: 10.1109/APEC.2015.7104490.
- [32] B. Lu, W. Liu, Y. Liang, F. C. Lee, and J. D. Van Wyk, “Optimal design methodology for LLC resonant converter,” in *Conference Proceedings - IEEE Applied Power Electronics Conference and Exposition - APEC*, 2006, vol. 2006, pp. 533–538, doi: 10.1109/apec.2006.1620590.
- [33] “A 90-w, high-efficiency, llc series-resonant converter withsecondary-side synchronous rectification - Recherche Google.” <https://www.google.com/search?client=firefox-b-d&q=A+90-w%2C+high-efficiency%2C+llc+series-resonant+converter+withsecondary-side+synchronous+rectification> (accessed Feb. 04, 2021).
- [34] G. Regnat, P. O. Jeannin, J. Ewanchuk, D. Frey, S. Mollov, and J. P. Ferrieux, “Optimized power modules for silicon carbide MOSFET,” in *ECCE 2016 - IEEE Energy Conversion Congress and Exposition, Proceedings*, 2016, doi: 10.1109/ECCE.2016.7855324.